Excited-state charging energies in quantum dots investigated by terahertz photocurrent spectroscopy

Y. Zhang, K. Shibata, N. Nagai, C. Ndebeka-Bandou, G. Bastard, and K. Hirakawa

Phys. Rev. B **93**, 235313 — Published 24 June 2016

DOI: 10.1103/PhysRevB.93.235313

Excited-state charging energies in quantum dots investigated by terahertz photocurrent spectroscopy

Y. Zhang[1,a)], K. Shibata[1,2,b)], N. Nagai[1], C. Ndebeka-Bandou[3,c)], G. Bastard[3], and K. Hirakawa[1,2,d)]

[1]*Institute of Industrial Science, University of Tokyo, 4-6-1 Komaba, Meguro-ku, Tokyo 153-8505, Japan*

[2]*Institute for Nano Quantum Information Electronics, University of Tokyo, 4-6-1 Komaba, Meguro-ku, Tokyo 153-8505, Japan*

[3]*Laboratoire Pierre Aigrain, Ecole Normale Superieure, 24 rue Lhomond F75005, Paris, France*

We have investigated the excited-state (ES) charging energies in quantum dots (QDs) by measuring a terahertz (THz)-induced photocurrent in a single electron transistor (SET) geometry that contains a single InAs QD between metal nanogap electrodes. A photocurrent is produced in the QD-SETs through THz intersublevel transitions and the subsequent resonant tunneling. We have found that the photocurrent exhibits stepwise change even within one Coulomb blockaded region as the electrochemical potential in the QD is swept by the gate voltage. From the threshold for the photocurrent generation, we have determined the charging energies for adding an electron in the photoexcited state in the QD. Furthermore, the charging energies for the ESs with different electron configurations are clearly resolved. The present THz photocurrent measurements are essentially dynamical experiments and allow us to analyze electronic properties in off-equilibrium states in the QD.

---

a) Electronic mail: zhangya@iis.u-tokyo.ac.jp.

b) Permanent address: Department of Electronics and Intelligent Systems, Tohoku Institute of Technology, Sendai 982-8577, Japan

c) Permanent address: Institute for Quantum Electronics, ETH Zurich, Auguste-Piccard-Hof 1, 8093 Zurich, Switzerland

d) Electronic mail: hirakawa@iis.u-tokyo.ac.jp.

In zero-dimensional nanostructures such as quantum dots (QDs) [1-3] , electrons are confined in a nanometer-scale volume and electron-electron interactions play important roles in determining their electronic and optical properties. Through single-electron capacitance spectroscopy [4-6] and single-electron tunneling measurements [7-11], one can determine charging energies as well as orbital energy separations in QDs. The charging energies, which arise from the Coulomb repulsion among electrons, can be determined from the Coulomb stability diagrams when an electron is added to the manybody ground states (GSs). However, since device operation always requires excitation of electrons, the Coulomb repulsion energies for excited states (ESs) are as important as those for the GSs.

Recently, we reported on terahertz (THz) intersublevel transitions in single InAs QDs [12-14]. By using a single electron transistor (SET) geometry that consisted of an InAs QD and nanogap metal electrodes coupled to a THz antenna, we could perform THz spectroscopy of a single InAs QD by measuring a photocurrent induced by intersublevel transitions and subsequent tunneling of photoexcited electrons [12]. From the THz-induced photocurrent distribution inside the Coulomb diamonds, it has been shown that there are two processes for the photocurrent generation, *i.e.*, the $N \leftrightarrow N$-1 excitation and $N \leftrightarrow N$+1 excitation; in the former process the photoexcited electron escapes the QD first, whereas in the latter process an electron from the electrodes first refills the empty state created by the photoexcitation [12]. Particularly, the refilling process in the $N \leftrightarrow N$+1 excitation process allows us to study the dynamics of electron charging to a photoexcited QD. We have found that the photocurrent peaks in the intersublevel transitions spectra for different ES configurations start growing at different gate voltages, which was attributed to the difference in the charging energies [12]. Here, we will show that the ESs charging energies can be quantitatively determined by the THz-induced photocurrent data.

In this work, we have investigated the charging energies for the ESs in the QDs by measuring the THz-induced photocurrent in QD-SETs. We have found that the photocurrent exhibits stepwise change even within one Coulomb blockaded region as the electrochemical potential in the QD is

swept by the gate voltage. From the threshold for the photocurrent generation, we have determined the charging energy for adding an electron in the photoexcited state, which is notably different from the charging energy for the GS determined from transport measurements. This difference originates from the difference in the orbital shapes for different shells, and cannot be explained by the commonly used constant capacitance model. Furthermore, in the multiple electron region, we have found that the charging energies for the ESs with different electron configurations can be clearly resolved as a stepwise-increase in the photocurrent. The present THz photocurrent measurements are essentially dynamical experiments and allow us to analyze electronic properties in off-equilibrium states in the QDs.

To understand the difference between the charging energies for the GSs and ESs, let us take a look at a schematic illustration of a Coulomb stability diagram for single electron tunneling, when spin-degenerate states are occupied by one electron, as shown in Fig. 1(a). The crossing point of the two transport conductance lines, P_1, corresponds to the condition that the electrochemical potential for the N-electron GS aligns with the Fermi level of the drain electrode and that for the (N+1)-electron GS aligns with the Fermi level of the source electrode (see Fig. 1(b)). Therefore, the source-drain voltage at P_1, $eV_{DS}(P_1)$, is equal to the charging energy when the QD makes a transition from the N-electron GS to the (N+1)-electron GS.

To study the charging energies for the ESs, we need to create an ES in the QD first. This can be done by using intersublevel excitations, as shown in Fig. 1(c). When the QD is illuminated with a THz radiation, an electron in the GS is excited to an upper energy state. Then, there are two possible processes for the system to return to the initial state; *i.e.*, the $N \leftrightarrow N$-1 excitation and the $N \leftrightarrow N$+1 excitation processes [12]. For the $N \leftrightarrow N$-1 excitation, the photoexcited electron tunnels out first and the electron number is reduced to N-1 in the intermediate state. Then, an electron in the electrodes fills the empty state created by the THz photoexcitation. In the $N \leftrightarrow N$+1 excitation, on the other hand, an electron in the electrodes first tunnels into the QD to fill the lower empty state and the electron number increases to N+1 in the intermediate state. Subsequently, the SET returns

to the initial state by emitting the photoexcited electron to the electrodes (Fig. 1(c)). Since the $N \leftrightarrow N$-1 excitation needs to have the photoexcited state above the Fermi levels of the electrodes, it produces a photocurrent in the pink colored region in the Coulomb diamond shown in Fig. 1(d). The size of the allowed region is set by the orbital energy difference, ΔE. Similarly, since the $N \leftrightarrow N$+1 excitation needs to overcome the charging energy E_C to add one more electron into the photoexcited QD, it produces a photocurrent in the blue colored region in the Coulomb diamond shown in Fig. 1(d). Note that the boundary of the blue colored region is set by the charging energy for the ESs.

When the photocurrent is dominated by the $N \leftrightarrow N$+1 excitation process, we can determine the required charging energy from the crossing point P_2 between the transport line (red solid line in Fig. 1(d)) and the threshold line for the photocurrent generation (red dashed line in Fig. 1(d)). Figure 1(e) shows the energy band diagrams at P_2. The transport line indicates the condition that the N-electron GS is aligned with the Fermi level of the drain electrode, whereas the photocurrent threshold line corresponds to the condition that the filled lower energy state in the $N \leftrightarrow N$+1 excitation is aligned with the Fermi level of the source electrode. Therefore, the chemical potential increase by adding one electron into the ES of the QD is equal to the Fermi energy difference between the source and drain electrodes, $eV_{DS}(P_2)$, which we will call the ES charging energy. Note that the charging energies for the GS and ESs are the same within the framework of the commonly-used constant capacitance model [15]. However, since actual orbital shapes are different for different shells, the ES charging energies are different from the GS charging energy and, furthermore, configuration-dependent.

The experiments were performed on the self-assembled InAs QDs grown by molecular beam epitaxy on semi-insulating (100) GaAs substrates. After successively growing a 300-nm-thick Si-doped GaAs layer, a 100-nm-thick undoped $Al_{0.3}Ga_{0.7}As$ barrier layer, and a 200-nm-thick undoped GaAs buffer layer, self-assembled InAs QDs were grown by depositing 4 monolayers of InAs at 480 °C. A pair of Ti(5 nm)/Au(15 nm) electrodes separated by a 20-nm-gap were directly placed

on an InAs QD and were used as the source and drain electrodes. The diameter of the QDs used in this experiment was about 80-100 nm. A backgate voltage, V_G, was applied to the Si-doped GaAs buffer layer to change the electrostatic potential in the QD. The THz light source used in this work was a globar placed in a Fourier transform spectrometer. To tightly focus the THz radiation onto the samples, a hyper-hemispherical Si lens was placed on the back surface of the samples. A bow-tie antenna structure was also implemented with the nanogap electrodes to concentrate the THz field in the nanogap region [16]. All the measurements were performed at 4.6 K. The experimental data shown in this paper were obtained for two samples, sample I and sample II, whose characteristics were partly presented elsewhere [19]. Here, we analyze the charging energies of the ESs by using the THz-induced photocurrent as a probe.

Figure 2(a) shows the Coulomb stability diagram of sample I. White solid lines are eyeguides for Coulomb diamonds. The numbers shown in the diamonds denote the number of electrons, N, in the QD. As seen in the figure, the Coulomb diamonds for the s- and p-shells are observed. The crossing point of the transport lines for N = 1 and 2 (point P_3) in Fig. 2(a) corresponds to the degeneracy condition for N = 1 and 2. Figure 2(c) shows the energy band diagram at point P_3. As seen in the figure, the Fermi energy difference at P_3 is equal to the charging energy for the N = 2 GS;

$$eV_{DS}(P_3) = 9.1 \pm 1 \text{ meV} \equiv E_C(\text{ss}). \quad (1)$$

Here, we use E_C(ss) to express the GS charging energy that originates from the Coulomb repulsion between two s-electrons.

The red curve in Fig. 2(b) shows the photocurrent measured as a function of V_G by applying a very small source-drain voltage (V_{DS} = 0.25 mV). This photocurrent is induced by the intersublevel transition of a 1s electron to the 2p state and subsequent tunneling. The positive photocurrent observed for -0.42 V < V_G < -0.36 V is induced by the $N \leftrightarrow N+1$ excitation process, because the

photocurrent has a large magnitude in the right corner of the $N = 1$ Coulomb diamond. The small negative photocurrent observed for -0.50 V < V_G < -0.42 V is caused by the $N \leftrightarrow N$-1 excitation process. The black curve shows the Coulomb oscillation peaks measured simultaneously with the photocurrent. Using the threshold for the THz photocurrent measured at $V_{DS} = 0$ and drawing a line in parallel with the N-electron GS conductance line, we can draw the threshold line for the $N \leftrightarrow N$+1 photocurrent generation, as shown by the red dashed line in the $N = 1$ diamond. Figure 2(d) shows the energy band diagram at the crossing point, P_4, of the transport line and the threshold line for the $N \leftrightarrow N$+1 excitation. We used the same tracing method also for the crossing points P_5, P_6 and P_7. The ES charging energy obtained at P_4 is equal to the Coulomb energy between an s-state electron and a p-state electron, as;

$$eV_{DS}(P_4) = 5.2 \pm 1 \text{ meV} \equiv E_C(sp). \quad (2)$$

Here, note that the ES for $N = 2$ can be either singlet or triplet. We have performed a simple numerical calculation, assuming that the QD has a two-dimensional, disk-shape geometry with a diameter of 50 nm. The geometry of the QD has been chosen to obtain the best fit to the experimental data for the charging energy of the $N = 1$ Coulomb diamond, $E_C(ss)$. Using the same model, we have estimated the charging energies, $E_C(sp)$, for the triplet and singlet ESs to be 5.1 meV and 10.6 meV, respectively [18]. The calculated triplet state Coulomb energy agrees well with the ES charging energy that we determined from the THz photocurrent.

Next, we apply the same technique to a multiple electron system, which has more electron configurations and the ES charging energies are, therefore, more complex than the two-electron case. Nevertheless, by using the THz photocurrent measurements, we can clearly resolve the charging energies for different ESs. Figure 3(a) shows the Coulomb stability diagram of sample II. The numbers shown in the diamonds denote the number of electrons, N, in the QD. The inset of Fig. 3(a) shows an SEM image of sample II. As seen, the QD is slightly elongated in the direction of the electrodes, *i.e.*, the [0-11] direction [17]. However, from Fig. 3(a), the Coulomb diamonds for $N =$

3, 4 and 5 have very similar addition energies (~15 meV), indicating that the energy splitting for the p-states caused by the shape anisotropy is rather small and is within the error bar of the present measurement. Therefore, in the following discussion we will neglect the orbital energy difference between p_- and p_+ states. Here, p_- and p_+ refer to the two p states whose degeneracies are slightly lifted by the small shape anisotropy of the QD. We use similar notations also for the d shells.

Figure 3(b) shows a blowup of the Coulomb diamond for $N = 6$ measured on sample II. The red curve in Fig. 3(c) shows a photocurrent induced by THz radiation measured as a function of V_G by applying $V_{DS} = 0.25$ mV. The black curve shows the Coulomb oscillation peaks measured simultaneously with the photocurrent. As seen in the figure, the photocurrent shows three stepwise increases with increasing V_G, indicating that multiple transitions participate in the photocurrent generation. Furthermore, since the photocurrent appears in the right corner of the Coulomb diamond, the observed photocurrent is generated by the $N \leftrightarrow N+1$ excitation process.

When $N = 6$, the optical selection rule allows three intersublevel transitions; namely, $p_- \rightarrow 2s$, $p_- \rightarrow d_-$, and $p_+ \rightarrow d_+$ transitions, because of the linearly polarized THz field caused by the antenna effect of the electrodes[12], as shown in Fig. 3(d). Figure 3(e) shows the photocurrent spectra measured at the three photocurrent steps. The main peak in spectrum I indicated by a pink arrow and the main peak of spectrum III indicated by a blue arrow give rise to shoulder-like features in spectrum II, whereas the main peak of spectrum II indicated by a red arrow forms a shoulder in spectrum III. This strongly suggests that there are three peaks in the photocurrent spectra and their intensities changes with V_G. From numerical fitting of the measured photocurrent spectra, we can indeed resolve three peaks that correspond to the three intersublevel transitions [12]. The slightly different linewidth of each transition in each spectrum suggests that the tunnel escape/refilling rates in the QD-SET slightly depend on V_G, although we do not know the detail at present. Note that the three peaks start growing at different gate voltages; *i.e.*, as V_G is increased, the $p_- \rightarrow 2s$ transition (pink) starts growing first. Then, the $p_- \rightarrow d_-$ transition (red) follows and the $p_+ \rightarrow d_+$ transition (blue)

grows at last. The observed behavior reflects the different charging energies required for electron addition to the photoexcited states.

Figures 4(a)-4(c) shows the energy band diagrams at the crossing points P_5, P_6 and P_7, respectively. As shown in Fig. 4(a), the Fermi energy difference at P_5 is equal to the charging energy when an electron in the electrodes fills the empty state created by the $p_- \rightarrow 2s$ transition,

$$E_C(p_- \rightarrow 2s) \equiv eV_{DS}(P_5) = 17 \pm 2 \text{ meV}. \quad (3)$$

Similarly, we can obtain the ES charging energies for the $p_- \rightarrow d_-$ and $p_+ \rightarrow d_+$ transitions.

$$E_C(p_- \rightarrow d_-) \equiv eV_{DS}(P_6) = 22 \pm 2 \text{ meV, and} \quad (4)$$

$$E_C(p_+ \rightarrow d_+) \equiv eV_{DS}(P_7) = 25 \pm 2 \text{ meV}. \quad (5)$$

Equations (3)-(5) show that we can quantitatively resolve the difference in charging energy for different electron configurations.

In summary, we have investigated the ES charging energies in QDs by measuring a THz-induced photocurrent in QD-SETs that contains a single InAs QD between metal nanogap electrodes. The photocurrent exhibits stepwise change even within one Coulomb blockaded region when the electrochemical potential in the QD is swept by the gate voltage. From the threshold for the photocurrent generation, we have determined the charging energy for adding an electron in a photoexcited state, which is notably different from the charging energy for the GS determined from transport measurements. This difference originates from the difference in the orbital shapes for different shells, and cannot be explained by the commonly used constant capacitance model. Furthermore, in the multiple electron region, we have found that the charging energies for the ESs with different electron configurations can be clearly resolved as a stepwise-increase in the

photocurrent. The present THz photocurrent measurements are essentially dynamical experiments and allow us to analyze electronic properties in off-equilibrium states in the QDs.

We thank Y. Arakawa for fruitful discussions and constant encouragement. This work was partly supported by CREST-JST, Grants-in-Aid from JSPS (No. 25246004, No. 25600013, and No. 26706002), MEXT Grant-in-Aid for Scientific Research on Innovative Areas "Science of hybrid quantum systems" (Grant No. 15H05868), Project for Developing Innovation Systems of MEXT, and research grants from the Canon Foundation and the Casio Science Foundation.

REFERENCES

[1] M. A. Kastner, Phys. Today **46**, 24 (1993).

[2] R. C. Ashoori, Nature **379**, 413 (1996).

[3] P. M. Petroff, A. Lorke, and A. Imamoglu, Phys. Today **54**, 46 (2001).

[4] R. C. Ashoori, H. L. Stormer, J. S. Weiner, L. N. Pfeiffer, S. J. Pearton, K. W. Baldwin, and K. W. West, Phys. Rev. Lett. **68**, 3088 (1992).

[5] P. Hawrylak, Phys. Rev. Lett. **71**, 3347 (1993).

[6] H. Drexler, D. Leonard, W. Hansen, J. P. Kotthaus, and P. M. Petroff, Phys. Rev. Lett. **73**, 2252 (1994).

[7] M. A. Kastner, Rev. Mod. Phys. **64**, 849 (1992).

[8] L. P. Kouwenhoven, Science **278**, 1788 (1997).

[9] S. Tarucha, D. G. Austing, T. Honda, R. J. van der Hage, and L. P. Kouwenhoven, Phys. Rev. Lett. **77**, 3613 (1996).

[10] S. M. Reimann and M. Manninen, Rev. Mod. Phys. **74**, 1283 (2002).

[11] M. Jung, T. Machida, K. Hirakawa, S. Komiyama, T. Nakaoka, S. Ishida, and Y. Arakawa, Appl. Phys. Lett. **87**, 203109 (2005).

[12] Y. Zhang, K. Shibata, N. Nagai, C. Ndebeka-Bandou, G. Bastard, and K. Hirakawa, Nano Lett. **15**, 1166 (2015).

[13] Y. Zhang, K. Shibata, N. Nagai, C. Ndebeka-Bandou, G. Bastard, and K. Hirakawa, Phys. Rev. B **91**, 241301 (2015).

[14] Y. Zhang, K. Shibata, N. Nagai, C. Ndebeka-Bandou, G. Bastard, and K. Hirakawa, Appl. Phys. Lett. **107**, 103103 (2015).

[15] C. W. J. Beenakker, Phys. Rev. B **44**, 1646 (1991).

[16] K. Shibata, A. Umeno, K. M. Cha, and K. Hirakawa, Phys. Rev. Lett. **109**, 077401 (2012).

[17] W. Ma, R. Nötzel, H.-P. Schönherr, and K. H. Ploog, Appl. Phys. Lett. **79**, 4219 (2001).

[18] See Supplemental Material for the calculation of the Coulomb energies of the singlet and triplet states in the QD.

[19] Sample I corresponds to sample A in ref. 13. Sample II corresponds to sample B in ref. 12.

Figure Captions

FIG. 1. (a) A schematic Coulomb stability diagram for single electron tunneling measurements. (b) The energy band diagrams for the crossing point P_{S1} in (a). (c) The energy band diagrams for $N \leftrightarrow N$-1and $N \leftrightarrow N$+1 photoexcitation processes. The processes are decomposed into three steps: initial, intermediate and final states. GS and ES stand for the ground and excited states, respectively. (d) The allowed regions for the $N \leftrightarrow N$-1and $N \leftrightarrow N$+1 photoexcitation processes are indicated in pink and blue, respectively. (e) The energy band diagrams at the crossing point P_{S2} between transport line and the photocurrent threshold line.

FIG. 2. (a) Coulomb stability diagram of sample I, which is replotted from Fig.1c of Ref. [13]. The inset shows an SEM image of sample I. The dot is marked by a red circle. White solid lines are eyeguides for the boundaries of the Coulomb diamonds. The number in the Coulomb diamonds denotes the number of electrons in the dot. White dashed lines denote the ESs. Red dashed line denotes the threshold line for photocurrent generation through $N \leftrightarrow N$+1 photoexcitation process. P_3 and P_5 indicate the crossing point of the two transport lines and that of the transport line and the photocurrent threshold line, respectively. (b) The red curve (I_P) shows THz-induced photocurrent as a function of V_G measured on sample I by applying a small source-drain voltage (V_{DS} = 0.25 mV) , which is a magnification of Fig. 1d of Ref. [13]. The black curve (I_{DS}) shows the Coulomb oscillation peaks measured simultaneously with the photocurrent. (c)-(d) Energy band diagrams at P_3 and P_4, respectively. E_C(ss) and E_C(sp) express the Coulomb energy between two s-state electrons and that between an s-state electron and a p-state electron, respectively.

FIG. 3. (a) Coulomb stability diagram of sample II, which is replotted from Fig. 1e of Ref. [12]. The inset shows an SEM image of sample II. The dot is marked by a red circle. White solid lines are eyeguides for the boundaries of the Coulomb diamonds. The number in the Coulomb diamonds denotes the number of electrons in the dot. (b) A blowup of the Coulomb diamond for N = 6. White dashed lines denote the threshold lines for photocurrent generation through the $N \leftrightarrow N$+1 excitation process. P_5 denotes the crossing points between the transport line and the photocurrent threshold

line for the $p_-\rightarrow 2s$ transition. Similarly, P_6 and P_7 denote the crossing point for the $p_-\rightarrow d_-$ and $p_+\rightarrow d_+$, respectively. (c) The red curve (I_P) shows the THz-induced photocurrent as a function of V_G by applying a small source-drain voltage (V_{DS} = 0.25 mV), which is a magnification of Fig. 1g of Ref. [12]. The black curve (I_{DS}) shows the Coulomb oscillation peaks measured simultaneously with the photocurrent. (d) Energy band diagram for N = 6. The THz field is polarized along the direction of the electrodes. Three possible transitions, *i.e.*, $p_-\rightarrow d_-$, $p_-\rightarrow 2s$, and $p_+\rightarrow d_+$, are indicated by red, pink, and blue arrows, respectively. (e) The photocurrent spectra measured at the three photocurrent steps. From the photocurrent spectra, we can clearly resolve three peaks by numerical fitting, corresponding to the three possible intersublevel transitions, *i.e.*, the $p_-\rightarrow 2s$, $p_-\rightarrow d_-$, and $p_+\rightarrow d_+$ transitions, which are indicated by pink, red, and blue curves, respectively.

FIG. 4 (a)-(c) Energy band diagrams at P_5, P_6, and P_7, respectively. $E_C(p_-\rightarrow 2s)$, $E_C(p_-\rightarrow d_-)$ and $E_C(p_+\rightarrow d_+)$ indicate the charging energies for the $p_-\rightarrow 2s$, $p_-\rightarrow d_-$ and $p_+\rightarrow d_+$ transitions, respectively.

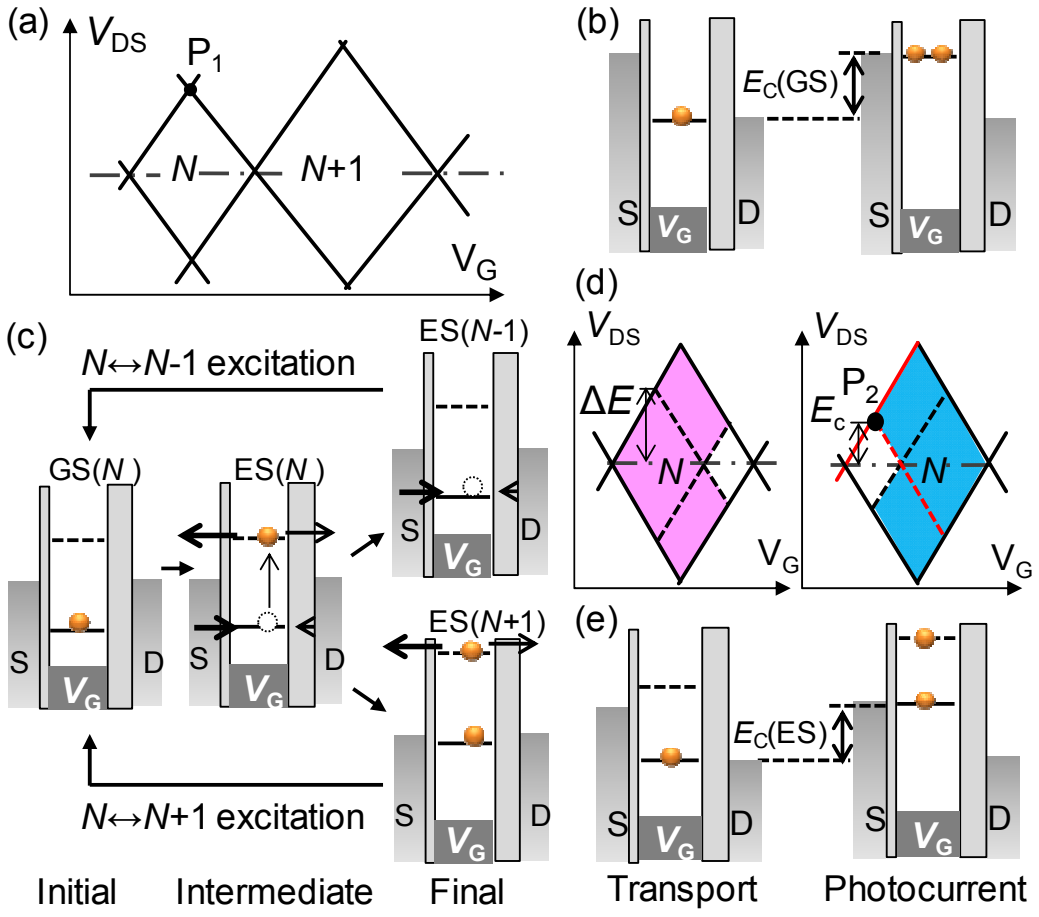
(a)
V_{DS}
P_1
N
N+1
V_G
(b)
E_C(GS)
S
V_G
D
(c)
$N\leftrightarrow N$-1 excitation
GS(N)
ES(N)
ES(N-1)
ES(N+1)
$N\leftrightarrow N$+1 excitation
Initial
Intermediate
Final
(d)
V_{DS}
ΔE
N
V_G
P_2
E_c
(e)
E_C(ES)
Transport
Photocurrent

FIG. 1.

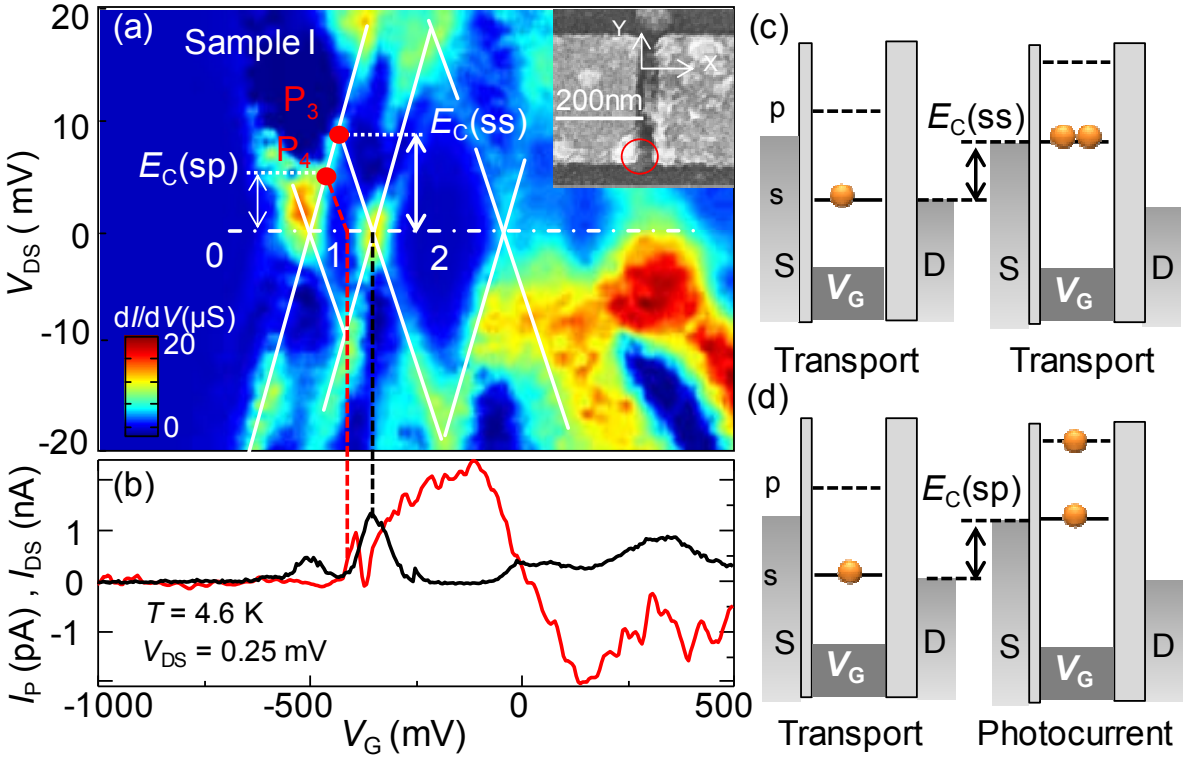
(a)
Sample I
P3
P4
EC(ss)
EC(sp)
0
1
2
dI/dV(μS)
20
0
200nm
Y
X
VDS (mV)
20
10
0
-10
-20
(b)
T = 4.6 K
VDS = 0.25 mV
IP (pA) , IDS (nA)
1
0
-1
-1000
-500
0
500
VG (mV)
(c)
p
s
S
VG
D
EC(ss)
Transport
Transport
(d)
EC(sp)
Transport
Photocurrent

FIG.2

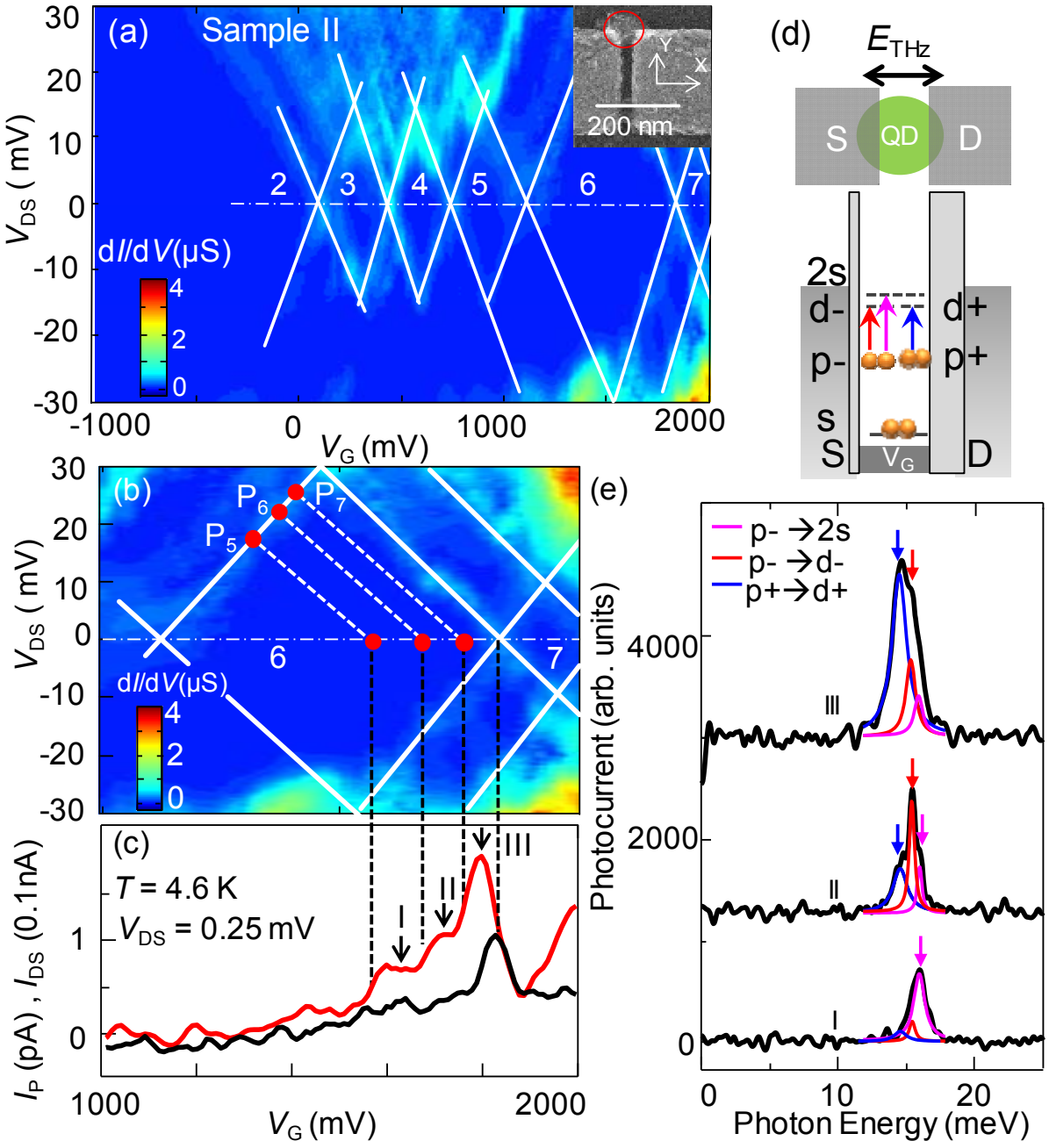
(a)
Sample II
200 nm
Y
X
2
3
4
5
6
7
dI/dV(μS)
4
2
0
30
20
10
0
-10
-20
-30
-1000
0
1000
2000
V_{DS} (mV)
V_G (mV)
(b)
P6
P7
P5
6
7
dI/dV(μS)
(c)
T = 4.6 K
V_{DS} = 0.25 mV
I
II
III
I_P (pA) , I_{DS} (0.1nA)
1000
2000
V_G (mV)
(d)
E_{THz}
S
QD
D
2s
d-
d+
p-
p+
s
S
V_G
D
(e)
p- →2s
p- →d-
p+→d+
4000
2000
0
Photocurrent (arb. units)
0
10
20
Photon Energy (meV)

FIG.3

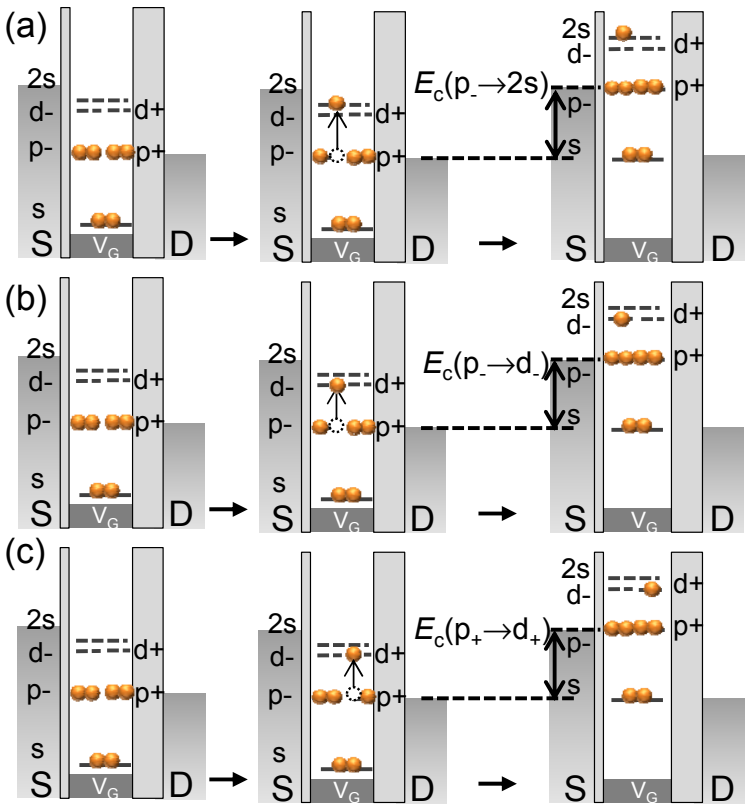
(a)
2s
d-
p-
s
d+
p+
S
V_G
D
$E_c(p_- \rightarrow 2s)$
(b)
$E_c(p_- \rightarrow d_-)$
(c)
$E_c(p_+ \rightarrow d_+)$

FIG. 4